Journal of
Materials Chemistry B

Materials for biology and medicine

Accepted Manuscript

This article can be cited before page numbers have been issued, to do this please use: I. Pandya, V. Joshi, R. Pansuriya, N. Raje, M. Assiri and N. Malek, *J. Mater. Chem. B*, 2025, DOI: 10.1039/D5TB00931F.

ROYAL SOCIETY OF CHEMISTRY

rsc.li/materials-b

View Article Online
DOI: 10.1039/D5TB00931F

Multifunctional IL@MOF Composite-Based Hydrogel for Enhanced Transdermal Drug Delivery of 5-Fluorouracil

Ishani Pandya[a], Vidhi Joshi[a], Raviraj Pansuriya[a], Naina Raje[b], Mohammed A. Assiri[c], Naved Malek[a]*

[a]Ionic Liquids Research Laboratory, Department of Chemistry, Sardar Vallabhbhai National Institute of Technology, Surat-395007, Gujarat, India

[b]Analytical Chemistry Division, Bhabha Atomic Research Centre, Trombay, Mumbai-400085, India

[c]Chemistry Department, Faculty of Science, King Khalid University, P.O. Box 9004, Abha 61413, Saudi Arabia

Corresponding Author e-mail: navedmalek@chem.svnit.ac.in

Abstract

Advances in biomaterial-based transdermal drug delivery systems (TDDS) are unlocking new possibilities for cancer therapy by enhancing skin permeability and enabling sustained drug release while minimizing systemic side effects. In this study, we developed a multifunctional hydrogel platform by encapsulating varying ratios of ionic liquids (ILs) into the micropores of judiciously selected metal-organic frameworks (MOFs), aiming to improve drug loading and delivery performance. Specifically, we utilized [TMG][Ol] IL, UiO-66-NH_2 MOF, and carboxymethyl cellulose sodium salt to fabricate a synergistic composite hydrogel. The resulting system demonstrated outstanding thermal stability, mechanical strength, adhesiveness, self-healing properties, and spreadability—key attributes for efficient TDDS applications. Biocompatibility assessments using HaCaT cells showed ~90% cell viability, confirming its cytocompatibility. Composite hydrogels prepared with [TMG][Ol]@UiO-66-NH_2 at ratios of 0.1:1 (G1) and 0.25:1 (G2) exhibited high drug-loading capacities of 671 mM and 397.8 mM for 5-fluorouracil (5-FU), respectively. *In vitro* transdermal drug penetration over 48 hours reached 76.4% for G1 and 82.7% for G2. Furthermore, cytotoxicity studies on A431 (epidermoid carcinoma) and MCF-7 (breast cancer) cancer cell lines confirmed the therapeutic potential of the drug-loaded hydrogels. Overall, the biocompatible [TMG][Ol]@UiO-66-NH_2-based hydrogel system offers a promising strategy for the transdermal delivery of hydrophilic anticancer agents, supporting its potential for future clinical translation in cancer therapy.

View Article Online
DOI: 10.1039/D5TB00931F

Keywords: Metal Organic Frameworks; Transdermal Drug Delivery; 5-Fluorouracil; Ionic Liquids; Hydrogel; Cancer Application

1. Introduction

Over the past few years, there has been surge of interest in noninvasive drug delivery methods, leading to significant attention on transdermal and topical drug delivery systems (TDDS) as promising alternatives to traditional routes like oral consumption or injections.[1] Advantages include avoiding enzymatic degradation, minimizing metabolic burden on the liver and diaphragm, extending therapeutic existence, and improving the response of patients to drugs.[2] The skin serves as an appealing route for transdermal drug delivery due to its ease of access and large surface area accessible for drug absorption. At the same time, the skin also work as a considerable barrier to drugs penetration, especially for high molecular-weight (> 500 Da) and hydrophilic molecules (Log P <0).[3] To alleviate this limitation, numerous solutions have been proposed, including physical methods like microneedles or electroporation ablation to reduce barriers and chemical compounds that promote permeability.[4] Chemical permeation enhancers including propylene glycols, sulfoxide, Tween 80, ethanol and menthol derivatives are commonly used to improve drugs penetrate on, however they can be hazardous and irritate the skin.[5] To overcome these, fatty acid-based permeation enhancers have been investigated more recently due to their low toxicity and minimal skin irritation.[6] In addition to these, the limited to no solubility of drugs, in particularly hydrophobic anticancer drugs in pharmaceutically approved solvents also hampers their applications as TDDS.[7] Ionic Liquids (ILs) with their tunable nature and wide range of polarity offers a tremendous potential in addressing all of these limitations offered by the conventional drug delivery routes.[8]

A number of attempts were made in the earlier studies to formulate IL-based TDDSs in different forms, such as lipid bilayers, emulsion-based systems, and micelles, to mention a few.[9] In earlier studies, hydrophobic ILs were synthesized using imidazolium as the cation and various anions, such as hexafluorophosphate and tetrafluoroborate, which proved to be effective skin

View Article Online
DOI: 10.1039/D5TB00931F

permeation enhancers. Lack of substantial biodegradability, questionable biocompatibility and limited encapsulation efficiencies as well as stability offered by these second generation ILs[10] are overcome through using recently developed fourth generation biocompatible fatty acid-based ILs (FAB-ILs) as TDDS in the form of microemulsion, vesicles,[11,12] ionogel[13] and hybrid hydrogel[14] improving both the skin permeation and solubility of drugs.[15] Further, integrating these FAB-ILs with recently developed Metal-organic frameworks (MOFs) will not only improve the drug loading efficiencies but also improve the stability of the hydrogel in addition to have the controlled release properties.[15] Here, the FAB-ILs get immobilized within the pores of a porous support of MOFs to integrate the advantages of both.[16] MOFs, a class of porous materials with high surface areas and tunable compositions, offer a promising support for ILs.[17] Loading ILs onto MOFs with porous structures to form IL@MOF nanohybrids, providing them with promising capabilities as drug carriers.[18] Embedding drug DOX and microwave (MW)-sensitive ILs [Bmim][PF_6] within the pores of ZIF-8 produced ZIF-8/DOX@ZrO_2@IL nanohybrids designed for the therapeutic effects against tumors.[19] Li et al. reported that MW-sensitive ILs were loaded onto MIL-101 (Fe) to prepare IL@MIL-101 (Fe) nanohybrids designed for microwave ablation of tumors.[20]

Among MOFs, Zirconium-based MOFs have shown exceptional biocompatibility, biodegradability, and chemical and thermal stability.[21] Amine functionalized zirconium-based dicarboxylate MOFs, UiO-66-NH_2 have been extensively explored as nanocarriers for the encapsulation and controlled release of drug molecules.[22] The NH_2 functional group strengthens the interaction between drug molecules and MOFs, leading to improved drug binding, loading and controlled release properties.[23] In TDDSs, the duration of skin contact is essential for enhancing drug penetration, thereby increasing the need for adhesiveness, self-healing ability and mechanical stability.[24]

In striving to develop smart TDDSs, in this study, we design hydrogels with exceptional biocompatibility, adhesiveness, mechanical properties, drug encapsulation capacity, responsiveness to external stimuli and has the ability to penetrate the drug through the SC layer of skin as the ideal solution for new age

View Article Online
DOI: 10.1039/D5TB00931F

TDDSs. The ILs used in this study consist of 1,1,3,3-tetramethylguanidine as the cation and Oleic acid as the anions, and are represented as [TMG][Ol]. We used UiO-66-NH_2 MOF, as MOFs composed of carboxylate linkers and cationic zirconium clusters, offer excellent potential as drug carriers due to their outstanding aqueous stability, high surface areas and significant loading capacity.[25] We have designed an IL@MOF-based polymeric hydrogel by incorporating [TMG][Ol]@UiO-66-NH_2 into a Carboxymethyl cellulose sodium salt-based matrix. The prepared hydrogel was employed to investigate the transdermal delivery of the anticancer drug 5-fluorouracil (5-FU), addressing the selective permeability of skin and the polarity of drug to facilitate its targeted delivery to infected cells while reducing potential side effects. This unique combination of IL@MOF composite and biopolymer holds great promise for TDDS applications, as the hydrogel can load drugs such as 5-FU, offering a wide range of possibilities in transdermal drug delivery.

2. Experimental work

2.1 Materials

1,1,3,3-tetramethylguanidine (TMG), carboxymethyl cellulose sodium salt (CMC-Na), PBS 7.0 and 5.2 buffer capsules were purchased from Sigma Aldrich. Zirconium chloride (>98.0%), 2-aminoterephthalic acid and 5-Fluorouracil (5-FU) were received from TCI (Tokyo Chemical Industry, Japan). Oleic acid was bought from SRL (Sisco Research Laboratory, India). The chemicals and reagents listed had purities over 99 % and were of analytical grade; they were used as they were supplied, requiring no further purification. Double-distilled deionized water was used throughout all experiment.

2.2 Preparation of [TMG][Ol]@UiO-66-NH_2 composite

The synthesis procedures for the pure [TMG][Ol] and pristine UiO-66-NH_2 are provided in the ESI. The IL@MOF composites were prepared using the wet impregnation method as previously described with minor modifications (**Scheme 1**).[26] The UiO-66-NH_2, in its purest form was activated by heating at 120 °C overnight under vacuum before incorporating the [TMG][Ol]. IL@MOF composites were prepared with varying IL ratios, ensuring that each was loaded to the maximum achievable level without leading to mud formation after solvent

View Article Online
DOI: 10.1039/D5TB00931F

removal. Accordingly, 20 mg and 50 mg of [TMG][Ol] were initially dissolved in 20 ml of ethanol with stirring for 1 hour at room temperature, as ethanol is used to dissolve the amino-functionalized basic IL.[27] Then, 200 mg of dehydrated UiO-66-NH_2 powder was added to the solution to prepare [TMG][Ol]@UiO-66-NH_2 ratios of 0.1:1 and 0.25:1. After the solvent was evaporated by stirring the mixture at 35 °C in open air, the resulting composites were dried overnight in an oven at 60 °C.

2.3 Preparation of hydrogel

To prepare the hydrogel (**Scheme 1**), a suspension of IL@MOF composites in the deionized water was initially prepared. In brief, A 2% w/v of [TMG][Ol]@UiO-66-NH_2 composite was added to the deionized water and thoroughly mixed using a magnetic stirrer to ensure an even dispersion of composite throughout the water. Ultrasonication was used for 30 minutes to improve the dispersion of particles. Following the addition of 2% CMC-Na, the mixture was heated to 35 °C using a magnetic stirrer until the CMC-Na was completely dissolved, forming hydrogel. The components utilized in this experiment for preparing the composites and hydrogels are shown in **Table 1**.

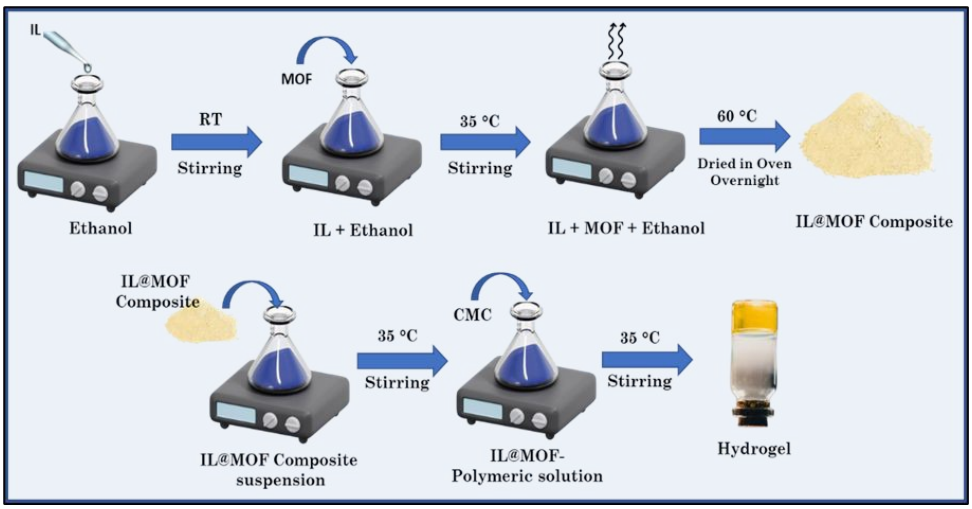

Scheme 1: Schematic representation of preparation of IL@MOF composites and hydrogel

Table 1. Composition used in the formation of hydrogels in the current study

Abbreviation	Molar ratio ([TMG][Ol]@UiO-66-NH_2)	IL@MOF Composite	CMC-Na	Remarks

[TMG][Ol]@UiO-66-NH_2 (0.1:1)	0.1:1	2%	-	Powder
[TMG][Ol]@UiO-66-NH_2 (0.25:1)	0.25:1	2%	-	Powder
[TMG][Ol]@UiO-66-NH_2 (0.1:1)	0.1:1	2%	1%	Viscous solution
[TMG][Ol]@UiO-66-NH_2 (0.25:1)	0.25:1	2%	1%	Viscous solution
G1	0.1:1	2%	2%	Gel
G2	0.25:1	2%	2%	Gel

2.4 Characterization of IL@MOF composites and hydrogels

Using the Brunauer–Emmett–Teller (BET) equation, the surface area and pore volume of the pristine MOFs and their IL@MOF composites were calculated using N_2 adsorption isotherms at 77.35 K. X-ray photoelectron spectroscopy (XPS) measurements were performed using a Thermoscientific NEXA Surface analyzer to analyze chemical composition within a range of 0 to 1350 eV. An X-ray diffractometer with monochromatic Cu-Kα (1.54056) radiation (40 kV, 30 mA) was used to analyze the X-ray diffraction (XRD) patterns. The diffractometer scanned within a 2θ range of 5-60° at a rate of 3° per minute. The Fourier transform infrared (FT-IR) spectra of [TMG][Ol], UiO-66-NH_2, [TMG][Ol]@UiO-66-NH_2 composites, CMC-Na and the prepared [TMG][Ol]@UiO-66-NH_2 based hydrogel were recorded using a Jasco6000 spectrophotometer to identify potential interactions responsible for gel formation. Small-angle neutron scattering (SANS) investigations were carried out at the Guide Tube Laboratory, Dhruva Reactor, Bhabha Atomic Research Centre in Mumbai, India, using a SANS-I diffractometer. We used SasView analytic software to investigate the experimental scattering data using a variety of fitting models. The thermal stability and decomposition characteristics of UiO-66-NH_2, [TMG][Ol], [TMG][Ol]@UiO-66-NH_2 composites, [TMG][Ol]@UiO-66-NH_2 based hydrogel were analyzed using thermogravimetric analysis (TGA). The samples were examined using the SDT Q600 V20.9 Build 20 TGA apparatus, which was heated

View Article Online
DOI: 10.1039/D5TB00931F

from 25 to 800 °C in an aluminum pan at a rate of 10 °C per minute with a nitrogen flow of 100 mL/min. To assess the thermal behavior, DSC analysis was conducted by cycling the temperature from 25 °C to 250 °C and back to 25 °C, at a constant heating and cooling rate of 10 °C/min. FE-SEM images of the UiO-66-NH_2, [TMG][Ol]@UiO-66-NH_2 composites, [TMG][Ol]@UiO-66-NH_2 based hydrogels and drug-loaded hydrogel were captured using a QUANTA 200 FESEM.

2.5 Mechanical property through Rheology

The properties of the hydrogels were examined using an Anton Paar Physica MCR 301 rheometer to analyze its mechanical attributes. Using a 40 mm diameter and 0.5 mm spacing, we used a parallel plate configuration with an attached transducer. A measurement of angular frequency sweep was performed over a range of 1–100 rad/s, while keeping a constant strain of 1%, to assess the rheological properties. At a constant frequency of 1 rad/s and with strain against modulus of G′ and G″ of 0–1%, the strain sweep analysis was evaluated. The viscosity of hydrogel was measured at shear rates ranging from 0 to 100(1/s).

Two glass slides (6 cm) of standard size were used to evaluate spreadability while accounting for the "slip" and "drag" characteristics of gel. After applying 2 g of hydrogel to one slide, a second slide was put on top of the gel, sandwiching it between the two slides. They scraped off the excess gel from the edges. The time (s) required for the top slide to move 6 cm was noted. This time interval reflects the gel's spreadability. Spreadability was calculated using the equation (1).

$$S = \frac{M*L}{T} \quad (1)$$

Where S stands for spreadability, M for weight, L for glass slide length moved, and T for time.

2.6 Drug loading study within the hydrogel

We used the swelling equilibrium approach, a reliable method, to load the 5-FU drugs (hydrophilic drug) into the hydrogel that had been prepared. Before being used, 17.5 mm dialysis membranes were immersed in distilled water for the whole night. A precisely measured amount of the hydrogel was then cautiously

View Article Online
DOI: 10.1039/D5TB00931F

placed into the dialysis membrane. For 24 hours at room temperature, this assembly was thereafter immersed in a predefined concentration of drug solution. The evaluation of the drug loading capacity in the hydrogel was carried out using drug absorption measurements. Using a standard calibration curve, we ascertained the loaded drugs (5-FU) concentration in the gel.

2.7 *In vitro* drug permeation studies

A Franz diffusion cell was used for skin penetration experiments, as previously mentioned.[28] After carefully removing the fat layer, the skin was sliced into 1.5x 1.5 cm pieces. After that, these skin pieces were put in the Franz diffusion cell, which contained 10 mL of phosphate buffer solution and was continuously shaken at 32 ± 1 °C, with the inner skin facing the receptor phase. The donor compartment, on the exterior side of the skin, was then covered with 0.5 g of the 5-FU-loaded hydrogel and protected with parafilm to avoid contamination. At regular intervals throughout a period of 48 hours, 0.25 mL samples were taken out of the receiving chamber. Following that, these samples were examined using UV-vis spectroscopy to ascertain the amount of 5-FU released at various intervals.

2.8 Stratum corneum (SC) study through FT-IR

The goat skin was taken out of the freezer and allowed to thaw for an hour at room temperature. After the top layer was removed, the goat skin was submerged in a trypsin solution and floated overnight to separate any dermal tissues from the SC. The SC was given a PBS wash and then allowed to dry at room temperature for 72 hours. After obtaining a control, FT-IR spectrum for a 0.5 cm x 0.5 cm SC of goat skin was recorded. Here, the sample was incubated with the examined material for duration of 24 hours. The next day, the sample was washed in PBS and allowed to air dry for 72 hours, another FT-IR spectrum for the SC of goat skin was obtained. This second spectrum was compared to the untreated SC spectrum in order to determine the impact of the test substance on the SC structure.

2.9 *In vitro* biocompatibility and cytotoxicity assay

The biocompatibility of the system was tested *in vitro* employing the MTT assay (3-(4,5-dimethylthiazol-2-yl)-2,5-diphenyltetrazolium bromide). A human

View Article Online
DOI: 10.1039/D5TB00931F

keratinocyte cell line (HaCaT) was used for the experiment. The cells (10,000 cells/well) were grown in a 96-well plate for 24 hours in DMEM media supplemented with 1% antibiotic solution and 10% FBS at 37 °C with 5% CO_2. Hydrogels at various concentrations were added in cell-filled wells for 48 hours. Cell viability was measured using the MTT test, and each concentration of hydrogel was compared to the positive control (without hydrogel). The same procedure was applied to assessed the cytotoxicity of the anticancer drug (5-FU)-loaded hydrogels in human epidermoid carcinoma (A431) and breast cancer (MCF-7) cell lines, with the goal of determining drug efficacy and IC_{50} values.

3. Results and Discussion

Integrating a judiciously designed biocompatible IL within the MOF can transform the IL@MOF composite by enhancing its stability, tunability, and functional properties. The IL plays a crucial role in modifying surface chemistry, improving guest molecule interactions, enhancing drug permeation and facilitating controlled drug release, making the system highly efficient for biomedical applications. However, the addition of excessive ILs causes the MOF (powder form) to become viscous and muddy, resulting in greater experimental uncertainties and also pore blockage within the MOFs.[29] Herein, we primarily investigate and analyzes the encapsulation of two [TMG][Ol] proportions (0.1 and 0.25) within the micropores of UiO-66-NH_2, to form [TMG][Ol]@UiO-66-NH_2 (0.1:1) and [TMG][Ol]@UiO-66-NH_2 (0.25:1).

The successful encapsulation of [TMG][Ol] within the microporous structure of UiO-66-NH_2 was demonstrated using N_2 adsorption/desorption tests (**Figure 1A**). With increasing the concentration of [TMG][Ol], the overall specific surface area decreases (**Table 2**).[27,30] The calculated BET surface areas of the prepared UiO-66-NH_2, [TMG][Ol]@UiO-66-NH_2 (0.1:1) and [TMG][Ol]@UiO-66-NH_2 (0.25:1) were 272.83 m²/g, 100.37 m²/g, and 5.62 m²/g, respectively, which are notably higher than those reported for [PP_{13}][TFSI]@NH_2-MIL-53(Al).[31] As the IL content in the UiO-66-NH_2 powder increased, a corresponding increase in

View Article Online
DOI: 10.1039/D5TB00931F

particle size was also observed, further confirming the successful encapsulating of [TMG][Ol] into the nano-micropores of UiO-66-NH_2.

Table 2: Total specific surface area, pore volume and pore radius for N_2 adsorption/desorption of different ratios of ILs

Sample	Surface area (m^2/g)	V_{total} (cc/g)	Pore radius (Å)
UiO-66-NH_2	272.83	0.15	<933.4
[TMG][Ol]@UiO-66-NH_2 (0.1:1)	100.37	0.057	<953.3
[TMG][Ol]@UiO-66-NH_2 (0.25:1)	5.62	0.010	<1108.8

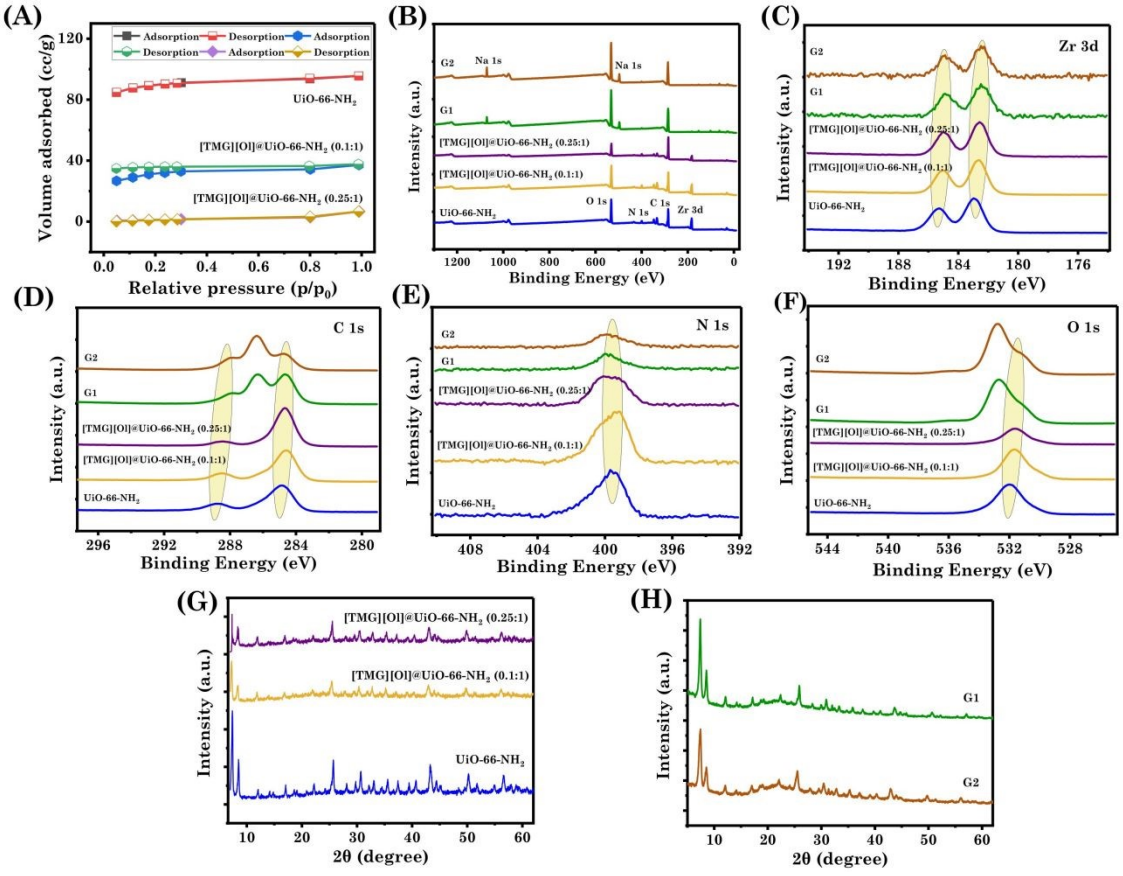

Figure 1: (A) N_2 adsorption desorption isotherms of UiO-66-NH_2 and UiO-66-NH_2-IL composites (B) Wide scan XPS spectra; High-resolution XPS

View Article Online
DOI: 10.1039/D5TB00931F

spectra of (C) Zr 3d (D) C 1s (E) N 1s (F) O 1s; PXRD of (G) MOF and IL@MOF composites (H) IL@MOF composites-based hydrogels

The elemental compositions and electronic interactions in the prepared materials were further examined using XPS analysis. The XPS spectrum of UiO-66-NH_2, both IL@MOF composites and both IL@MOF composite hydrogel contains clear peaks associated with C 1s, N 1s, O 1s and Zr 3d electrons (**Figure 1B**). We confirmed the coexistence of Zr, C, N and O element peaks at 182.2, 284, 399.1 and 531.5 eV in all materials. Additionally, the binding energy peaks observed at 1071 and 497 eV in the spectra of both hydrogel (G1 and G2) can be attributed to the sodium (Na 1s, 1071 eV and Auger peaks at 497 eV), resulting from the addition of carboxymethyl cellulose sodium salt, to prepare the hydrogel. The XPS atomic content data, shown in **Table S1**, indicates an increase in nitrogen atom content in [TMG][Ol]@UiO-66-NH_2 composites, attributed to the presence of the amine group in the [TMG][Ol].

The high-resolution Zr 3d XPS spectrum shows peaks at 185.44 and 183.07 eV, corresponding to Zr^{4+} $3d_{3/2}$ and $3d_{5/2}$ energy levels (**Figure 1C**) in UiO-66-NH_2 and [TMG][Ol]@UiO-66-NH_2 based composites.[33] These peaks are shifted to higher binding energies compared to those in UiO-66-NH_2 in the hydrogel samples. In the C 1s XPS spectrum of UiO-66-NH_2 and [TMG][Ol]@UiO-66-NH_2 based composites we observed two distinct peaks at 288.7 (C=O) and 284.8 eV (C–C, C=C, C–H). However when characterized for hydrogel samples, i.e. in G1 and G2, we observed one additional peak at 286.3 eV, may be associated with carbon in C–O and C–O–C groups (**Figure 1D**).[32] The N 1s spectrum displays peak at 399.4 eV, attributed to the nitrogen in the $-NH_2$ group (**Figure 1E**).[33] The O 1s spectrum of the UiO-66-NH_2 and both IL@MOF composites show a single peak at 531.6 eV, while in the G1 and G2 hydrogel, two distinct peaks are observed at 531.6 and 532.7 eV, corresponding to the oxygen of the C=O and C–O (O–C–O and C–OH), respectively (**Figure 1F**).[34] In all the spectra discussed above, a slight shift to lower binding energies is observed, indicating a strong interaction between the UiO-66-NH_2 and [TMG][Ol], as well as between the [TMG][Ol]@UiO-66-NH_2 composite and CMC-Na.

View Article Online
DOI: 10.1039/D5TB00931F

The crystalline nature of the synthesized UiO-66-NH_2 and its modifications with IL was examined using XRD analysis (**Figure 1G**). The pristine UiO-66-NH_2 exhibited characteristic diffraction peaks corresponding to its well-defined crystalline framework, confirming the successful synthesis of a highly ordered porous structure. Sharp diffraction peaks at 2θ=7.5˚ and 8.5˚, which correspond to the (111) and (002) planes, further indicated the formation of pure UiO-66-NH_2 MOF nanoparticles.[35] Modification with the [TMG][Ol] decreases the intensity, but the integrity is not greatly affected. However, the retention of diffraction peaks suggested that the structural integrity of the UiO-66-NH_2 was largely preserved. The formation of IL@MOF-based hydrogel further altered the diffraction pattern, showing broadening of peaks, which can be attributed to the amorphous nature of the polymeric network and the dispersion of [TMG][Ol]@UiO-66-NH_2 within the hydrogel matrix (**Figure 1H**). With an increase in [TMG][Ol] concentration in the composites ([TMG][Ol]@UiO-66-NH_2 (0.25:1)) and hydrogel (G2), the peak intensity decreased further, indicating a gradual loss of crystallinity. This reduction can be attributed to the disruption of the UiO-66-NH_2's long-range order due to [TMG][Ol] incorporation, which may lead to partial pore filling, or interactions between [TMG][Ol] and UiO-66-NH_2, thereby affecting its structural integrity.

Building on the prior study, the FT-IR spectra were used to analyzed the chemical interactions and functional groups within the material (**Figure 2A**). In the spectra of [TMG][Ol], a broad band at 3350–3290 cm^{-1} corresponds to N–H stretching, which validates the existence of the C=NH_2^+ cationic group. Olefinic C-H stretching in ILs occurs about 3005 cm^{-1}. Sharp peaks at 2925–2850 cm^{-1} suggest C–H stretching of methyl and methylene units. Two bands—symmetric stretching at 1441–1401 cm^{-1} and asymmetric stretching at 1598–1553 cm^{-1}—confirm the carboxylate anion. C=C stretch combined with C=N is observed around 1655 cm^{-1}, from this spectrum, from these, the successful synthesis of the [TMG][Ol] is confirmed.[36]As for UiO-66-NH_2, broad peaks at 3450 and 3250 cm^{-1} confirm the presence of the N–H bond of the amino group in 2-aminoterephathalic acid. At 1259 cm^{-1}, the peak indicates the C–N bonds of aromatic amines. Characteristic bands were assigned to the carboxyl group from

View Article Online
DOI: 10.1039/D5TB00931F

2-aminoterephathalic acid at 1375 cm^{-1}, 1426 cm^{-1}, and 1561 cm^{-1}. The Zr-O bond is responsible for the absorption bands at 763 and 685 cm^{-1}, and all of the distinctive peaks that were seen were consistent with those that had been reported in the literature.[37]

For the composite, a blue shift from 3203 cm^{-1} to 3343 cm^{-1} was detected, likely caused by strong hydrogen bonding or electrostatic interactions between the $–NH_2$ groups of UiO-66-NH_2 and $[Ol]^-$ in the [TMG][Ol]. Broadening in the N–H stretching region (around 3200 cm^{-1}) indicates hydrogen bonding between $[TMG]^+$ and the $–NH_2$ groups of MOFs. A slight shift of the carboxylate –C=O stretching band of the MOF in the composite can indicate strong interaction with [TMG][Ol].

To analyze hydrogel formation, we examined hydrogel spectra with their IL@MOF composites and gelator. In both G1 and G2 hydrogels, shifts in the -OH and -CO peaks indicate strong hydrogen bonding interactions between the [TMG][Ol]@UiO-66-NH_2 composites and CMC-Na. The hydrogels spectra closely resemble those of the IL@MOF composites, with an additional new peak at 1027 cm^{-1} attributed to the C–O–C bond of the CMC-Na, while the N–H band from UiO-66-NH_2 merges with the O–H band. The Zr–O bond observed at 763 and 685 cm^{-1} in both the [TMG][Ol]@UiO-66-NH_2 composites and the hydrogels (G1 and G2) confirms the stability and intact presence of the UiO-66-NH_2 structure.

Furthermore, SANS analysis was carried out on hydrogel samples before and after drug loading to investigate the internal structure and to understand the structural changes induced by drug incorporation. For the G1 and G2 hydrogels, the scattering data were well-fitted using the mass fractal model, indicating a self-similar, loosely connected network structure (**Figure 2B**). S(Q) in the context of mass fractal structure may be obtained using equation (2)

$$S_{mf}(Q) = 1 + \frac{1}{(QR_b)^{D_m}} \frac{D_m \Gamma(D_m - 1)}{\left[1 + (Q\xi)^{-2}\right]^{(D_m-1)/2}} \sin\left\{(D_m - 1) \times \tan^{-1}(Q\xi)\right\} \quad (2)$$

where ξ signifies the maximum length up to which fractal microstructure exists, R_b denotes the building block size and D_m is the mass fractal dimension.

View Article Online
DOI: 10.1039/B5TB00931F

In the G2 hydrogel, a decrease in the building block radius along with an increase in the fractal dimension was observed, suggesting a transition toward a more compact and densely cross-linked network, likely due to an increase in [TMG][Ol] concentration that enhances molecular interactions and network tightening as shown in **Table 3**. The parameter Dm serves as a measure of the openness of fractal structures, where a value of 1 indicates loosely connected aggregates, and a value of 3 corresponds to densely packed aggregates.[38] While the scattering profiles of the drug-loaded hydrogels were better fitted with the correlation length model, [39] indicating the presence of short-range structural correlations rather than a fractal-like arrangement.

$$I(Q) = \frac{A}{Q_m} + \frac{C}{(1+ Q\xi^m)} + B \quad (3)$$

The Porod function, the first component in this formula, characterizes the clustering of the gel structure at large length scales. The incoherent background is B, and the Porod exponent m describes the hydrogel's fractal aspect. The second term is the Lorentzian function; in particular, the Lorentzian exponent is the inverse of the Floury exponent, and the correlation length of the polymer chains is represented by ξ. This change in the fitting model indicates that drug encapsulation induces a structural reorganization within the gel matrix (**Figure 2C**). The corresponding fitting parameters are presented in **Table 3**.

Table 3: Fitting parameters of hydrogels before and after drug loading.

Before drug loading	**Building block radius (Å)**	**Fractal dimension Dm**	**Model**
G1	5.93	1.52	Mass fractal
G2	5.10	2.15	Mass fractal
After drug loading	**Correlation length (Å)**	**Power coefficient**	
5-FU@G1	2.98	3.68	Correlation length
5-FU@G2	1.82	3.45	Correlation length

View Article Online
DOI: 10.1039/D5TB00931F

Thermal stability of the synthesized [TMG][Ol], UiO-66-NH_2, [TMG][Ol]@UiO-66-NH_2 composites and hydrogels were evaluated through TGA. As shown in **Figure 2D**, three phases of weight loss are observed in the pure UiO-66-NH_2. The evaporation of absorbed water is the cause of the first weight loss, which occurs between 50 and 100 °C. The second weight-loss stage is then produced in the 160–260 °C range by the loss of the remaining DMF molecules in the MOF. It exhibits a gradual degradation phase between 300 and 550 °C. After that, MOF crystallinity is lost as the MOF breaks down into tetragonal zirconia.[40,41] In the [TMG][Ol], a gradual mass loss was observed between 60 °C and 200 °C, followed by a sharp decline, with the material remaining stable up to 300 °C. The TGA of the [TMG][Ol]@UiO-66-NH_2 composites revealed a mass loss pattern similar to that of the pristine UiO-66-NH_2, indicating comparable thermal behavior with distinct variations due to the incorporation of the [TMG][Ol]. The weight loss of both composites is primarily attributed to the evaporation of solvent molecules. We observed that the [TMG][Ol]@UiO-66-NH_2 composite exhibited greater thermal stability compared to both the pristine [TMG][Ol] and the UiO-66-NH_2 (**Figure 2D**). In the IL@MOF composite hydrogel, the initial weight loss up to 100 °C is primarily due to the evaporation of water. The hydrogel remained stable up to 300 °C, after which a sharp mass loss was observed, attributed to the degradation of the CMC-Na.[42] Overall, the IL@MOF-based hydrogel demonstrates enhanced thermal stability as compare to their pristine forms.

The remarkable thermal stability of both the UiO-66-NH_2 (**Figure 2E**) and the hydrogels (**Figure 2F**) was further confirmed by DSC analysis. The DSC thermograms exhibited no significant endothermic or exothermic transitions up to 100 °C, indicating the absence of any thermal degradation or phase transitions within this temperature range. These results corroborate the TGA findings and further establish the thermal robustness of the developed system for drug delivery applications.

View Article Online
DOI: 10.1039/D5TB00931F

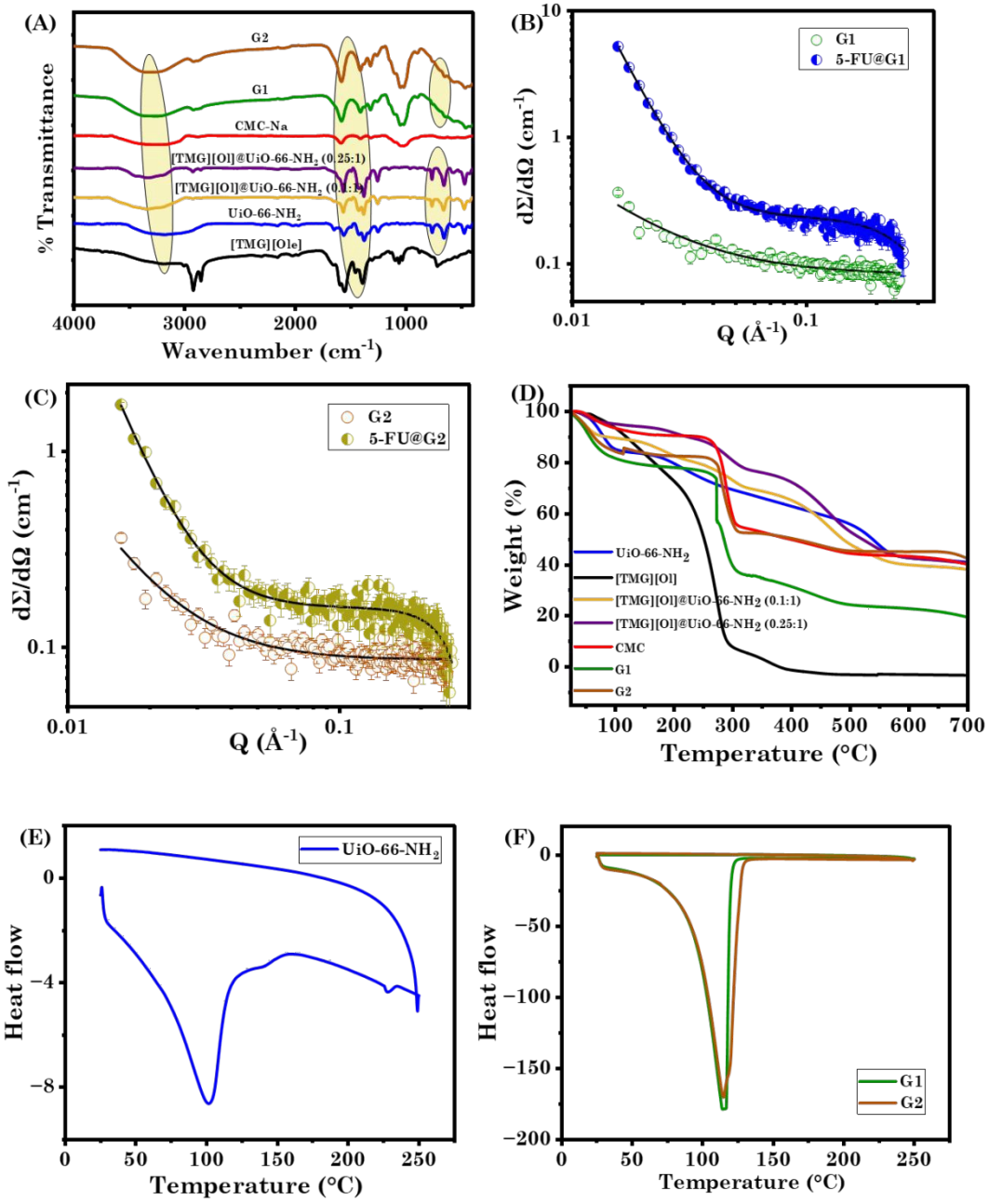

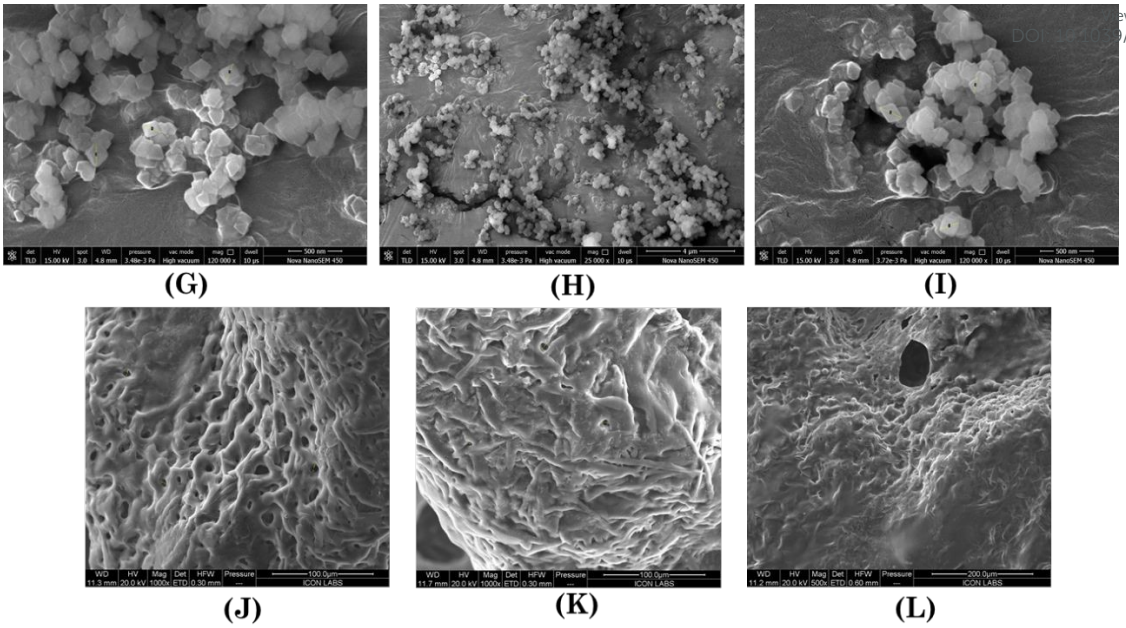

Figure 2: (A) FT-IR spectra of pure components and prepared composites and hydrogels; SANS graph of (B) G1 and 5-FU@G1 (C) G2 and 5-FU@G2 (D) TGA curve of MOF, IL, IL@MOF composites and hydrogel; DSC curve of (E) UiO-66-NH_2 (F) G1 and G2; FE-SEM images of (G) UiO-66-NH_2 (H) [TMG][Ol]@UiO-66-NH_2 (0.1:1) (I) [TMG][Ol]@UiO-66-NH_2 (0.25:1) (J) G1 (K) G2 (L) 5-FU@G1

Further, the surface morphology and microstructural characteristics of the pure MOF, IL-MOF composites, IL@MOF-based hydrogel and drug loaded IL@MOF-based hydrogel were analyzed through FE-SEM. As shown in **Figure 2G**, the octahedron UiO-66-NH_2 was effectively constructed with regular crystal faces and a relatively uniform dimension with average size of 188 nm. The morphology of the studied UiO-66-NH_2 is similar to that observed by Zhang et al.[43] Even after the incorporation of IL, i.e. [TMG][Ol]@UiO-66-NH_2(0.1:1) and [TMG][Ol]@UiO-66-NH_2(0.25:1), the composites maintained a consistent octahedral shape with average size of 212 and 266 nm, respectively (**Figure 2H,I**). This finding suggested that structure of MOF was preserved during the modification process. **Figure 2J,K** shows highly porous, interconnected network structure characteristic of hydrogels, facilitating drug encapsulation and release. The hydrogel matrix indicated that pores in G1 and G2 gel were uniformly distributed and had average sizes of 6.2 and 5.6 μm, respectively. The hydrogel

View Article Online
DOI: 10.1039/D5TB00931F

surface exhibits a rough texture, indicating the incorporation of [TMG][Ol]@UiO-66-NH_2 composite within the polymer matrix. The incorporation of IL@MOF composite in the hydrogel is confirmed by the characterization results, which reveal the dispersion of distinct nanocrystals throughout the hydrogel matrix. The drug-loaded hydrogel has a slightly more irregular surface than the unloaded hydrogel, which is most likely caused by the interaction of the 5-FU molecules with the [TMG][Ol]@UiO-66-NH_2 composite (**Figure 2L**). The pores are distributed, with an average size of 3.5 μm, incorporation of the 5-FU slightly reduces the overall porosity of the hydrogel compared to the drug-free hydrogel.

Rheological analyses were used to evaluate the mechanical strength of hydrogels, presenting important information about their viscoelastic behavior and mechanical characteristics.[14,44] The mechanical strength of the hydrogel under study was investigated through measurements of angular frequency sweep. The analysis revealed variations in the storage moduli (G') and loss moduli (G") as a function of angular frequency at 25 °C, as depicted in **Figure 3A**. The findings show that, for constant strain of 0.1%, the storage modulus (G′) continuously exceeds the loss modulus (G″) throughout a broad frequency range, i.e., up to 100 rad/s. This phenomenon can be elucidated by the robust colloidal forces present within the gel networks.

To determine the viscoelastic behavior of hydrogels, the strain sweep test was conducted. Crossover points (γ_c) for G1 and G2 hydrogels were found at 8.3 and 10.8% strain values, respectively, as shown in **Figure 3B**. The higher strain values observed in the G2 hydrogel attributed to the higher concentration of the [TMG][Ol] within the hydrogel matrix. The area below γ_c where G′ is greater than G″ is referred to as an elastic or linear region. The hydrogel acts like a semisolid material in this region. Above γ_c, G′ is less than G″, indicating that the hydrogel distorted and behaved like a viscous solution. The strain sweep data shows that hydrogels exhibit viscoelastic characteristics.

Viscosity study is essential in drug delivery systems to understand hydrogel behavior during treatment. High viscosity can lead to obstructions and difficulties, whereas low viscosity could hinder drugs delivery. The study found

View Article Online
DOI: 10.1039/D5TB00931F

that increasing the shear rate from 0.1 to 100 s^{-1}, we observed reduction in the viscosity of the hydrogel (**Figure 3C**). The hydrogels flow with an increasing shear rate, as seen by the steady shear flow (flow curve). At low shear rates, hydrogels exhibit shear-thinning behaviour, maintaining a relatively high viscosity that causes a sharp rise in shear stress. Shear-thinning in the hydrogels indicates decreased viscosity because shear stress increases at a diminishing pace as shear rate increases (**Figure 3D**).

For the hydrogel to be an intelligent TDDD, it has to exhibit self-healing properties. We used a conventional visual observation technique, in which circular gels were placed close together, to evaluate the self-healing capabilities of the hydrogel under investigation. These two hydrogel fragments seemed to self-heal after five minutes, and a single piece formed (**Figure 3E**). The result was confirmed by stretching using a pair of tongs, and it was seen that the hydrogel did not break particularly where it had healed. The entire procedure demonstrates that the hydrogel can self-heal without the need of outside stimuli.

To achieve optimal therapeutic benefits, it is essential that hydrogels possess good spreadability when applied to the skin or specific target areas. At room temperature, the G1 and G2 hydrogels exhibit average spreadability values of 19.16 ± 0.9 and 20.12 ± 1.1 g.cm/s, respectively. These results suggest the application and possible therapeutic effects of the hydrogel by influencing its spreadable behaviour.

For TDDSs, adhesive behaviour is crucial because the period of time a drug is in contact with the skin has a significant influence on drug penetration. Because of its non-covalent interactions with the substrates, the investigated hydrogel was tested for its capacity to form bonds with a variety of biological systems, including the skin, as well as hard surfaces, including rubber, steel, plastic and glass (**Figure 3F**).[13] Functional groups like NH_2, OH and COO^- provide hydrogel its adhesive properties and are in charge of the noncovalent interactions with other functional groups on the surface of these materials.[45] Underwater adhesiveness is essential for transdermal drug delivery, ensuring extended skin contact and sustained drug release even in moist conditions. This characteristic was assessed by testing the adhesive strength of the hydrogel in

an aqueous condition (**Figure 3G**). Strong adherence was shown by the hydrogel even when water was present, indicating that it might be used in physiological conditions in a stable and efficient manner. This feature improves drugs penetration and sustains prolonged contact, making it more appropriate for transdermal drug delivery.

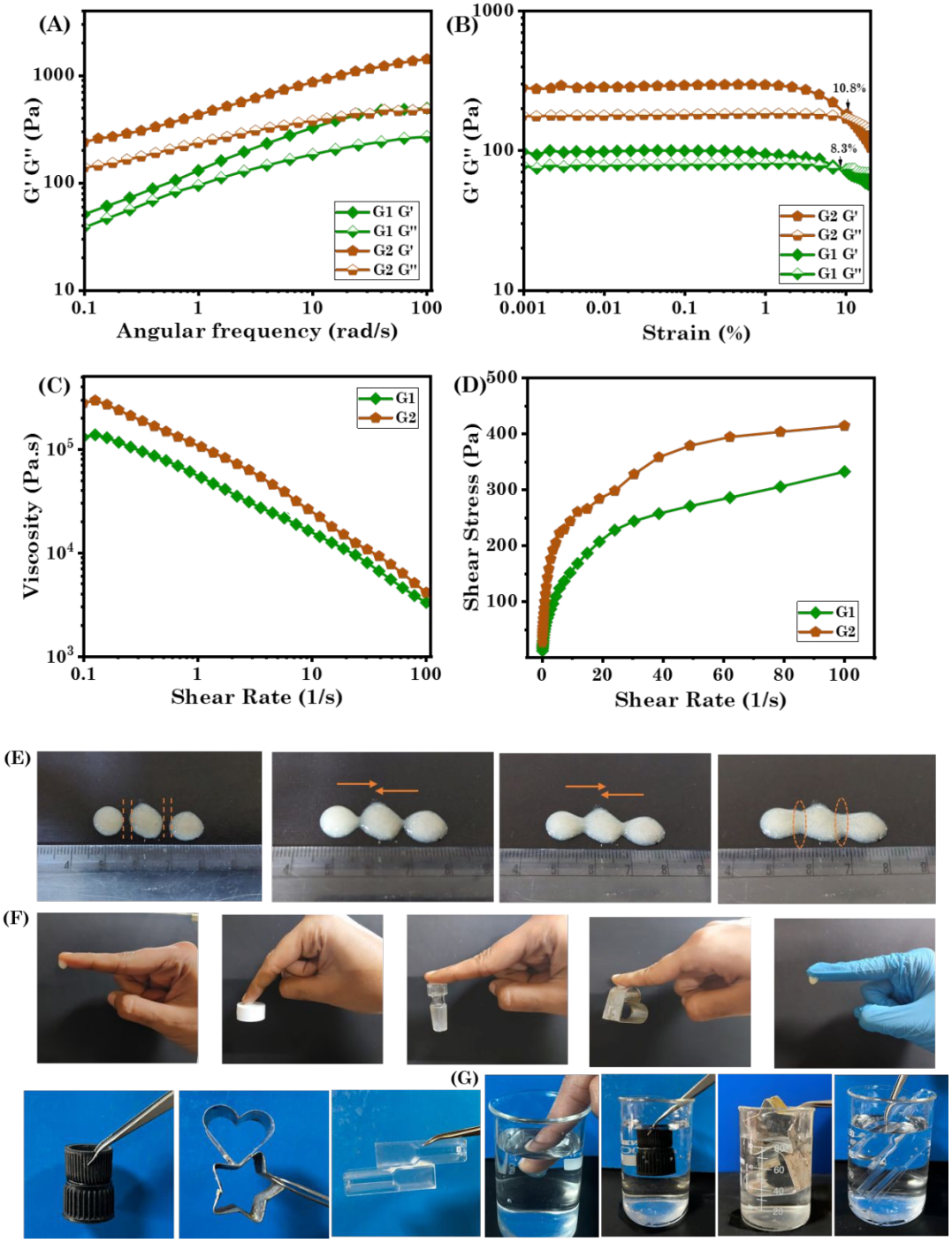

View Article Online
DOI: 10.1039/D5TB00931F

Figure 3: (A) Frequency sweep data of hydrogels at constant strain 0.1 % (B) Strain sweep with a constant frequency of 1 rad/s (C, D) Viscosity measurement (E) Visual images of self-healing capability of gel (F) Adhesive characteristics with skin, rubber, plastic, glass and metal (G) Adhesive properties in aqueous environment

3.8 *In vitro* biocompatibility assay with HaCaT cells

Assessing material compatibility is critical for DDSs to ensure safety and efficacy. The biocompatibility of the G1 and G2 hydrogels was evaluated using the HaCaT cell line at a concentration of 1000 µg/mL, revealing 91.94% and 91.29% cell viability, respectively (**Figure 4A**). This noteworthy outcome shows that the hydrogel is highly biocompatible, which is extremely promising for its possible uses in drug delivery and skin tissue creation. This is attributed to the use of biocompatible materials in the formation of hydrogels, including UiO-66-NH_2, [TMG][Ol], and CMC-Na.[11,46,47] The control image of HaCaT cells is shown in **Figure 4F**, and the cell viability after 48 hours of treatment with a IL@MOF based hydrogel is shown in **Figure 4G,H**.

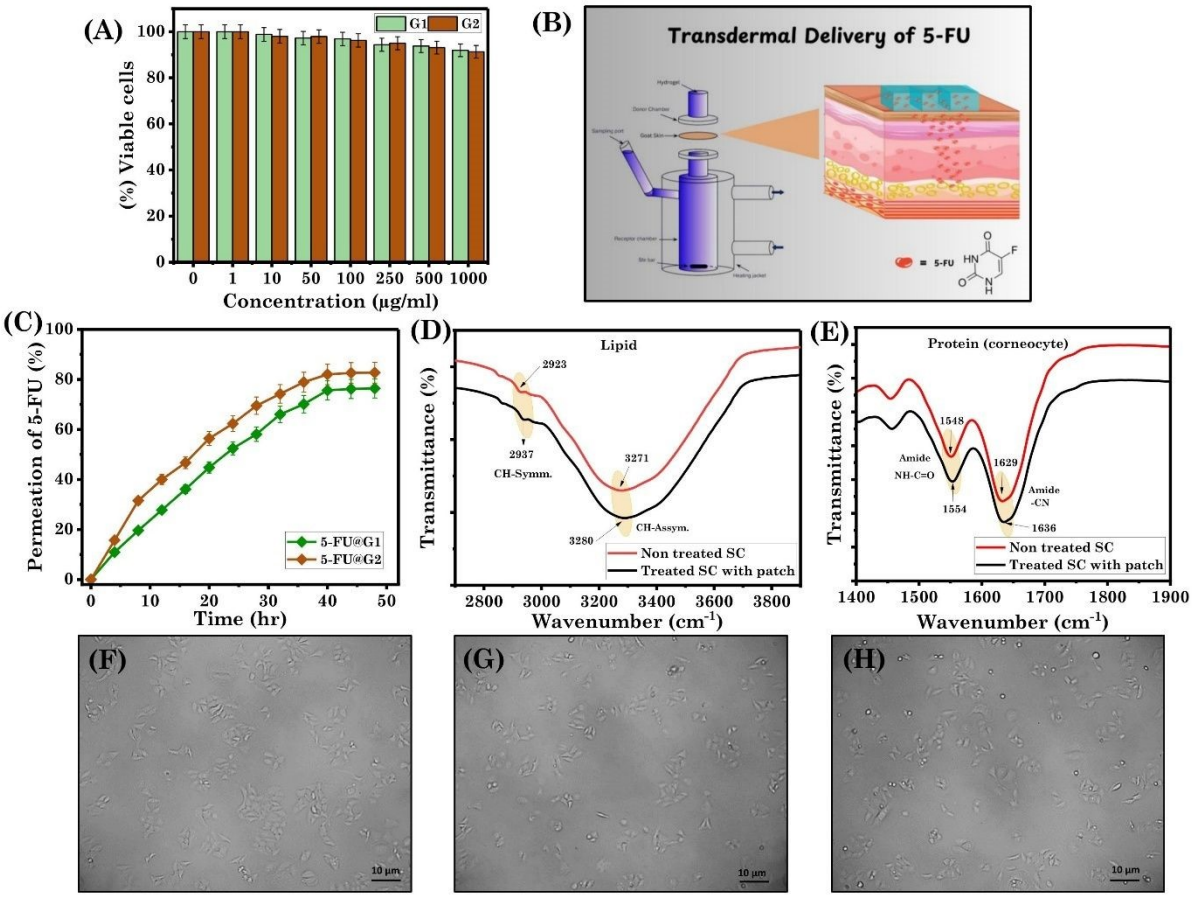

View Article Online
DOI: 10.1039/D5TB00931F

Figure 4: (A) HaCaT (%) cell viability (B) Schematic representation of transdermal drug delivery using a Franz diffusion cell (C) Permeation of 5-FU as a function of time at pH 7.4; FT-IR spectrum of SC before and after treatment with drug loaded patch (D) Lipid (E) Protein (F) HaCaT control; after 48 h (G) G1 (H) G2

3.9 Drug (5-FU) loading profile and *in vitro* permeation study of 5-FU in the hydrogel

Hydrogels have shown great promise in the loading and delivery of anticancer drug like 5-FU. Hydrogels are ideal for drug administration in cancer treatment and wound healing because of their special qualities, which include their capacity for self-healing and their adherence to the matrix and skin. In this research, we especially investigated the capacity of hydrogels to load the anticancer drugs 5-FU. 5-FU is a robust anticancer drug that interrupts DNA synthesis and limits cancer cell proliferation.[48] The drug loading capacity of 5-FU in G1 and G2 is 671 mM and 397.8 mM, respectively, corresponding to approximately 4-fold and 3-fold increases compared to the hydrogel without [TMG][Ol]@UiO-66-NH_2. This significant enhancement highlights the remarkable drug loading efficiency of the hydrogel. The higher drug loading capacity observed in G1 compared to G2 can be attributed to the greater surface area and pore volume of the [TMG][Ol]@UiO-66-NH_2 (0.1:1) composite used in G1. In contrast, the increased [TMG][Ol] content in G2 likely led to pore blockage within the UiO-66-NH_2 structure, thereby limiting the available sites for drug encapsulation. Furthermore, the enhancement in solubility is also due to non-covalent interaction present, i.e., hydrogen bonding, electrostatic interaction, π-π Stacking, steric interaction and pore confinement.

To successfully penetrate drugs molecules via the skin, the SC barrier must be surpassed.[49] Drugs must have a molecular weight of less than 500 Da, a considerable lipophilicity (log octanol–water partition coefficient between 1 and 3), and a melting point of less than 200 °C in order to pass through skin.[50] Since 5-FU has a log octanol–water coefficient of −0.89, which makes penetration challenging,[51] we overcome this problem through encapsulating 5-FU in

View Article Online
DOI: 10.1039/D5TB00931F

hydrogels. Using goat skin, we examined the *in vitro* skin penetration of 5-FU through the Franz diffusion cell at 32 °C and 48 hours (**Figure 4B**). Goat skin is used because its biological properties are comparable to those of human skin.[52] Under normal physiological conditions (pH 7.4), the 5-FU permeation percentages for 5-FU@G1 and 5-FU@G2 hydrogels are found to be 76.4% and 82.7% respectively (**Figure 4C**). As oleic acid serves as a penetration enhancer in both systems, both exhibit high permeation of 5-FU through the skin. However, since the [TMG][Ol] concentration is higher in 5-FU@G2, we observed a greater permeation in this system. In general, the majority of fatty acids have a good ability to improve skin penetration.[53] There is one unsaturation in oleic acid in the form of a π-bond, which may form π−π interactions with the SC layer, improves drugs penetration through the skin.[54] Both hydrogels exhibited these interactions, which led to better skin penetration as compared to conventional skin penetration enhancers like Tween-80 and other CPE.[55] These results imply that hydrogels based on [TMG][Ol]@UiO-66-NH_2 have the potential to deliver drugs through the skin.

In TDD, the SC layer of the skin acts as a barrier, preventing drugs entry.[56] Subsequently, FT-IR analysis was conducted to identify changes in the intracellular lipid content within the SC. In general, lipid fluidization and/or lipid extraction from the SC layer are responsible for the enhanced skin permeability of drug molecules.[57] The shift in the CH_2 symmetric and CH_2 asymmetric stretching vibrations at 2858 and 2931 cm^{-1}, respectively, and/or the decrease in the lipid peak area around 2858 cm^{-1} suggest that lipid fluidization and lipid extraction occurred in the SC layer.[58] Additionally, the characteristic keratin peaks for NH-C=O str. were shifted from 1548 cm^{-1} to 1554 cm^{-1} and from 1629 cm^{-1} to 1636 cm^{-1} respectively, indicating that the keratin structure is damaged following patch incubation and revealing details about the protein structure in SC (**Figure 4D,E**). These findings allow us to conclude that the drug enters the body by: i) disrupting the lipid bilayers of SC; and ii) altering the structure of the keratin protein. By doing this, it is decreasing the skin barrier characteristics of SC, which improves the permeation of drug into the skin.

View Article Online
DOI: 10.1039/D5TB00931F

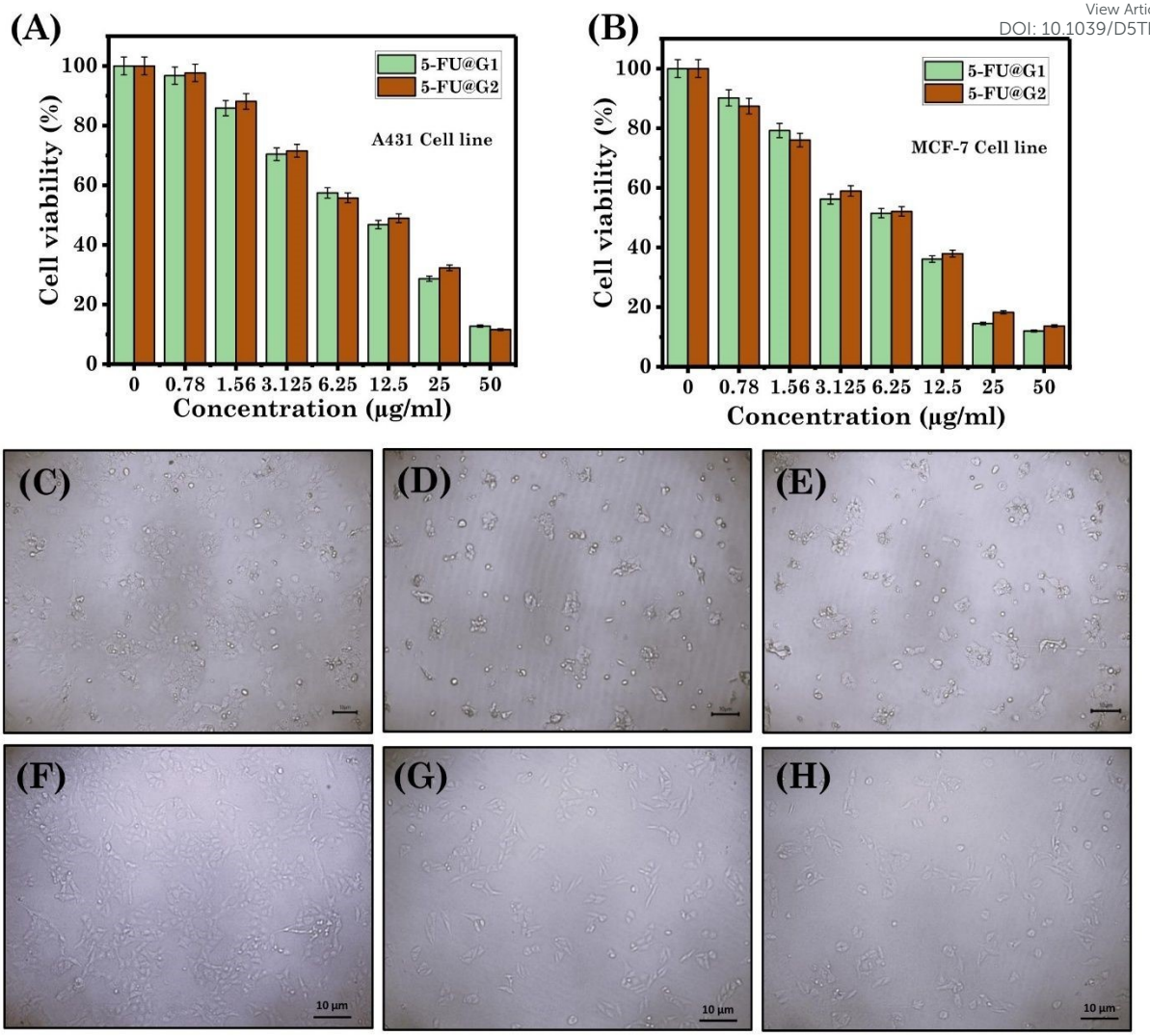

Figure 5: *In vitro* cytotoxicity of 5-FU loaded hydrogels on the (A) A431 cell line (B) MCF-7 cell line; Images of A431 cell line (C) Control; After treatment (D) 5-FU@G1 (E) 5-FU@G2; Images of MCF-7 cell line (F) Control; After treatment (G) 5-FU@G1 (H) 5-FU@G2

3.10 *In vitro* cytotoxicity of hydrogels

The 5-FU-free hydrogels demonstrated outstanding biocompatibility, showing minimal cytotoxicity toward normal cells, data *vide supra*. An *in vitro* cytotoxicity research was used to ascertain the efficacy and dosage needed for 5-FU-loaded hydrogels for tumor cell inhibition.[59] For this purpose, we employed cell lines, specifically A431 (skin cancer) and MCF-7 (breast cancer). The IC_{50} values obtained for the 5-FU@G1 hydrogel after 48 hours were 11.65 µg/mL for the A431 cell line and 6.44 µg/mL for the MCF-7 cell line, as illustrated in **Figure**

View Article Online
DOI: 10.1039/D5TB00931F

5A,B. Similarly, the IC_{50} values for the 5-FU@G2 hydrogel were 12.23 μg/mL and 6.51 μg/mL for the A431 and MCF-7 cell line respectively (**Figure 5A,B**). These results imply that systems have good cytotoxicity against malignant cell lines at lower dosages (**Figure 5**).

4. Conclusions

In the present manuscript, we have successfully synthesized the [TMG][Ol]@UIO-66-NH_2 composites through incorporating different concentrations of the [TMG][Ol]. The IL@MOF composites were then transformed into the hydrogel matrix using CMC-Na as the gelator. As such prepared hydrogels can be used as the potential multifunctional system for the advanced drug delivery applications, offering a promising combination of structural stability, excellent biocompatibility and enhanced drug-loading and permeation efficacy. We compared the effects of different ratios of [TMG][Ol] into the micropores of UiO-66-NH_2 on their drug delivery performance, thermal stability and drug permeation capability. We have prepared successfully two different IL@MOF-based hydrogels through synergistically interacting [TMG][Ol]@UiO-66-NH_2 composites with CMC-Na and analyzed them using BET, XPS, PXRD, FT-IR, SANS, TGA, DSC and FE-SEM techniques. The IL@MOF based hydrogel demonstrated several advantageous properties, including strong mechanical strength, self-healing, self-adhesion and spreadability, making it a promising candidate for TDD applications. The hydrogels demonstrated excellent *in vitro* biocompatibility, with cell viability remaining above 90% for HaCaT cells after 48 hours of treatment with various hydrogel concentrations. Hydrogels improved the permeability of the hydrophilic drugs 5-FU through the skin by increasing the fluidity of the intracellular lipid in the SC layer. Among both hydrogels, hydrogel with higher [TMG][Ol] loading exhibit greater skin permeability. *In vitro* cytotoxicity data showed that 5-FU-loaded hydrogels had a potent anticancer effect on A431 and MCF-7 cell lines, even at lower dosages. In conclusion, the IL@MOF-based hydrogels, with their enhanced skin permeability and biocompatibility, present a promising approach for effective TDD, paving the way for future advancements in targeted therapeutic applications.

View Article Online
DOI: 10.1039/D5TB00931F

Author contributions

Ishani Pandya: Conceptualization, methodology, writing-original draft and visualization.

Vidhi Joshi: Methodology and writing-original draft

Raviraj Pansuriya: Methodology and writing-original draft

Naina Raje: Methodology and writing-original draft

Mohammed A. Assiri: Methodology and writing-original draft

Naved I. Malek: Conceptualization, Supervision, writing-review and editing, funding acquisition.

All authors have given approval to the final version of the manuscript.

Keywords: Metal Organic Frameworks; Transdermal Drug Delivery; 5-Fluorouracil; Ionic Liquids; Hydrogel; Cancer Application

Conflicts of interest

There are no conflicts to declare.

Data availability

Data will be made available on request.

Acknowledgments

NM acknowledges the financial assistance from Board of Research in Nuclear Sciences (BRNS) with Sanction No: 58/14/10/2024-BRNS and UGC-DAE-CSR for the Collaborative Research Scheme (UDCSR/MUM/AO/CRS-M-997/2023). The authors gratefully acknowledge Dr. Debes Ray and Dr. Vinod K. Aswal for providing access to the SANS instrument facility at the Solid-State Physics Division, Bhabha Atomic Research Centre, Trombay, Mumbai, India.

5. References

1 W. Y. Jeong, M. Kwon, H. E. Choi and K. S. Kim, *Biomater. Res.*, 2021, **15**.

2 A. Alkilani, M. T. McCrudden and R. Donnelly, *Pharmaceutics*, 2015, **7**, 438–470.

3 M. R. Prausnitz and R. Langer, *Nat. Biotechnol.*, 2008, **26**, 1261–1268.

4 D. Ramadon, M. T. C. McCrudden, A. J. Courtenay and R. F. Donnelly, *Drug Deliv. Transl. Res.*, 2022, **12**, 758–791.

5 I. Pathan and C. Setty, *Trop. J. Pharm. Res.*, 2009, **8**.

6 S. A. Ibrahim and S. K. Li, *Pharm. Res.*, 2010, **27**, 115–125.

7 A. Alkilani, M. T. McCrudden and R. Donnelly, *Pharm.*, 2015, **7**, 438–470.

8 R. Pansuriya, T. Patel, K. Singh, A. Al Ghamdi, N. Kasoju, A. Kumar, S. K. Kailasa and N. I. Malek, *Int. J. Biol. Macromol.*, 2024, **277**, 134112.

9 R. Md Moshikur, I. M. Shimul, S. Uddin, R. Wakabayashi, M. Moniruzzaman and M. Goto, *ACS Appl. Mater. Interfaces*, 2022, **14**, 55332–55341.

10 S. N. Pedro, C. S. R. Freire, A. J. D. Silvestre and M. G. Freire, *Int. J. Mol. Sci.*, 2020, **21**, 8298.

11 I. Pandya, S. Mishra, T. Patel, N. Keppeler, S. Kumar, V. K. Aswal, S. Kumar Kailasa, O. El Seoud and N. I. Malek, *J. Mol. Liq.*, 2024, **409**, 125443.

12 M. Jain, H. Ukani, S. Kumar, V. K. Aswal, S. K. Kailasa, O. A. El Seoud and N. I. Malek, *ChemistrySelect*, 2024. 9, e202303162.

13 R. Pansuriya, J. Doutch, B. Parmar, S. K. Kailasa, N. Mahmoudi, C. Hoskins and N. I. Malek, *J. Mater. Chem. B*, 2024, **12**, 5479–5495.

14 H. Ukani, N. Parsana, S. Mehra, A. Kumar, I. Khan, M. A. Assiri and N. Malek, *ACS Appl. Eng. Mater.*, 2024, **2**, 2583–2596.

15 R. Md Moshikur, Md. R. Chowdhury, H. Fujisawa, R. Wakabayashi, M. Moniruzzaman and M. Goto, *ACS Sustain Chem. Eng.*, 2020, **8**, 13660–13671.

16 Y. Yao, X. Zhao, G. Chang, X. Yang and B. Chen, *Small Struct.*, 2023, **4**, 2200187.

17 I. Pandya, O. A. El Seoud, M. A. Assiri, S. Kumar Kailasa and N. I. Malek, *J. Mol. Liq.*, 2024, **395**, 123907.

18 L.-Y. Li, Y.-R. Gao, R. Xue, Y. Shu, J.-H. Wang and Z.-J. Wang, *J. Mater. Chem. B*, 2023, **11**, 6491–6515.

19 L. Su, Q. Wu, L. Tan, Z. Huang, C. Fu, X. Ren, N. Xia, Z. Chen, X. Ma, X. Lan, Q. Zhang and X. Meng, *ACS Appl. Mater. Interfaces*, 2019, **11**, 10520–10531.

20 L.-Y. Li, Y.-R. Gao, R. Xue, Y. Shu, J.-H. Wang and Z.-J. Wang, *J. Mater. Chem. B*, 2023, **11**, 6491–6515.

21 J. B. DeCoste, G. W. Peterson, H. Jasuja, T. G. Glover, Y. Huang and K. S. Walton, *J. Mater. Chem. A*, 2013, **1**, 5642.

22 N. Rabiee, M. Bagherzadeh, M. Heidarian Haris, A. M. Ghadiri, F. Matloubi Moghaddam, Y. Fatahi, R. Dinarvand, A. Jarahiyan, S. Ahmadi and M. Shokouhimehr, *ACS Appl. Mater. Interfaces*, 2021, **13**, 10796–10811.

23 Z. Li, S. Zhao, H. Wang, Y. Peng, Z. Tan and B. Tang, *Colloids Surf., B*, 2019, **178**, 1–7.

24 H. Pitakjakpipop, R. Rajan, K. Tantisantisom, P. Opaprakasit, D. D. Nguyen, V. A. Ho, K. Matsumura and P. Khanchaitit, *Biomacromolecules*, 2022, **23**, 365–376.

25 N. Rakhshani, N. Hassanzadeh Nemati, A. R. Saadatabadi and S. K. Sadrnezhaad, *J. Drug Deliv. Sci. Technol.*, 2021, **66**, 102881.

26 Ö. Durak, H. Kulak, S. Kavak, H. M. Polat, S. Keskin and A. Uzun, *J. Phys.: Condens. Matter*, 2020, **32**, 484001.

27 I. Pandya, O. A. El Seoud, M. A. Assiri, S. Kumar Kailasa and N. I. Malek, *J. Mol. Liq.*, 2024, **395**, 123907.

28 N. Parsana, O. El Seoud, A. Al-Ghamdi, N. Kasoju and N. Malek, *ChemistrySelect*, 2024, **9**, e202304157.

29 H. F. Xiang, B. Yin, H. Wang, H. W. Lin, X. W. Ge, S. Xie and C. H. Chen, *Electrochim. Acta*, 2010, **55**, 5204–5209.

30 M. Zeeshan, V. Nozari, M. B. Yagci, T. Isık, U. Unal, V. Ortalan, S. Keskin and A. Uzun, *J. Am. Chem. Soc.*, 2018, **140**, 10113–10116.

31 S. Wang, Y. Liu, L. He, Y. Sun, Q. Huang, S. Xu, X. Qiu and T. Wei, *Chin. J. Chem. Eng.*, 2024, **69**, 47–55.

32 X. Chen, X. Wang and D. Fang, *Fullerenes, Nanotubes Carbon Nanostruct.*, 2020, **28**, 1048–1058.

33 X. Zhao, G. Chang, H. Xu, Y. Yao, D. Dong, S. Yang, G. Tian and X. Yang, *ACS Appl. Mater. Interfaces.*, 2024, **16**, 7364–7373.

34 Y. Peng, Z. Chen, R. Zhang, W. Zhou, P. Gao, J. Wu, H. Liu, J. Liu, A. Hu and X. Chen, *Nanomicro. Lett.*, 2021, **13**, 192.

35 N. Rakhshani, N. Hassanzadeh Nemati, A. Ramazani Saadatabadi, S. K. Sadrnezhaad, *Int. J. Eng.*, 2021, **34**, 1874-1881.

36 P. K. Khatri, A. M.S., G. D. Thakre and S. L. Jain, *Mater. Sci. Eng.: C*, 2018, **91**, 208–217.

37 H. M. Khalid, A. Mujahid, A. Ali, A. L. Khan, M. Saleem and R. M. Santos, *Int. J. Energy Res.*, 2024.

38 S. K. Agrawal, N. Sanabria-DeLong, P. R. Jemian, G. N. Tew and S. R. Bhatia, *Langmuir*, 2007, **23**, 5039–5044.

39 B. Hammouda, D. L. Ho and S. Kline, *Macromolecules*, 2004, **37**, 6932–6937.

40 Z. Li, C. Liu, J. J. Frick, A. K. Davey, M. N. Dods, C. Carraro, D. G. Senesky and R. Maboudian, *Carbon N Y*, 2023, **201**, 561–567.

41 J. Shanahan, D. S. Kissel and E. Sullivan, *ACS Omega*, 2020, **5**, 6395–6404.

42 B. Kumar, R. Priyadarshi, Sauraj, F. Deeba, A. Kulshreshtha, K. K. Gaikwad, J. Kim, A. Kumar and Y. S. Negi, *Gels*, 2020, **6**, 49.

43 Y.-Y. Zhang, W. Xu, J.-F. Cao, Y. Shu and J.-H. Wang, *Anal. Chim. Acta.*, 2021, **1147**, 144–154.

44 I. Pandya, S. Kumar, V. K. Aswal, O. El Seoud, M. A. Assiri and N. Malek, *Int. J. Pharm.*, 2024, **658**, 124206.

45 H. Jung, M. K. Kim, J. Y. Lee, S. W. Choi and J. Kim, *Adv. Funct. Mater.*, 2020, **30**, 2004407.

46 E. P. Yalcintas, D. S. Ackerman, E. Korkmaz, C. A. Telmer, J. W. Jarvik, P. G. Campbell, M. P. Bruchez and O. B. Ozdoganlar, *Pharm. Res.*, 2020, **37**, 33.

47 W. Pan, W. Wang, P. Wang, D. Chen, S. Liu, L. Zhang, Z. Wang, H. Yang, Y. Xie, F. Huang, G. Zhou and B. Wang, *Mater. Des.*, 2024, **238**, 112688.

48 B. Pardini, R. Kumar, A. Naccarati, J. Novotny, R. B. Prasad, A. Forsti, K. Hemminki, P. Vodicka and J. Lorenzo Bermejo, *Br. J. Clin. Pharmacol.*, 2011, **72**, 162–163.

49 R. Neupane, S. H. S. Boddu, M. S. Abou-Dahech, R. D. Bachu, D. Terrero, R. J. Babu and A. K. Tiwari, *Pharmaceutics*, 2021, **13**, 960.

50 T. Jiang, T. Wang, T. Li, Y. Ma, S. Shen, B. He and R. Mo, *ACS Nano*, 2018, **12**, 9693–9701.

51 M. A. Safwat, G. M. Soliman, D. Sayed and M. A. Attia, *Mol. Pharm.*, 2018, **15**, 2194–2205.

52 R. Neupane, S. H. S. Boddu, J. Renukuntla, R. J. Babu and A. K. Tiwari, *Pharmaceutics*, 2020, **12**, 152.

53 Md. R. Islam, Md. R. Chowdhury, R. Wakabayashi, N. Kamiya, M. Moniruzzaman and M. Goto, *Pharmaceutics*, 2020, **12**, 392.

54 Y. Funakoshi, Y. Iwao, S. Noguchi and S. Itai, *Chem. Pharm. Bull.,* 2015, **63**, 731–736.

55 R. Pansuriya, T. Patel, S. Kumar, V. K. Aswal, N. Raje, C. Hoskins, S. K. Kailasa and N. I. Malek, *ACS Appl. Bio. Mater.*, 2024, **7**, 3110–3123.

56 D. Yang, C. Liu, D. Ding, P. Quan and L. Fang, *Int. J. Pharm.*, 2021, **602**, 120560.

57 A. Banerjee, K. Ibsen, Y. Iwao, M. Zakrewsky and S. Mitragotri, *Adv. Healthc. Mater.*, 2017, **6**, 1601411.

58 R. Md Moshikur, I. M. Shimul, S. Uddin, R. Wakabayashi, M. Moniruzzaman and M. Goto, *ACS Appl. Mater. Interfaces*, 2022, **14**, 55332–55341.

59 M. A. Safwat, G. M. Soliman, D. Sayed and M. A. Attia, *Mol. Pharm.*, 2018, **15**, 2194–2205.

View Article Online
DOI: 10.1039/D5TB00931F

Data availability

Data will be made available on request.